ADVANCED MATERIALS TECHNOLOGIES
www.advmattechnol.de

Tunable Subtractive Structural Colors Enabled by Phase-Change Metasurfaces

Ruhao Pan, Chensheng Li, Zhiyang Tang, Junhao Tan, Bo Wang, Haifang Yang, and Junjie Li**

Structural colors originating from the metasurface show irreplaceable advantages in high resolution, long-term stability, and vivid displays. However, the reconfigurable regulation of the structural color metasurface remains challenging for that once the structure of the metasurface is fixed, the optical response is also determined. Here, structural color metasurfaces are designed and experimentally demonstrated, composed of a metallic reflector and sandwiched nanopillars based on the phase change material Sb_2S_3. Abundant colors are obtained by tuning the critical dimensions of the nanoresonator for what determines the response frequency of the magnetic dipoles, which manifests a reflection dip (absorption peak) in the spectrum curve. Most importantly, the on-off of displacement current during the phase change process also results in a distinctive reflectance and thus provides the basis for the active color control. Cyan, magenta, and yellow are taken as examples, and it is verified that the structural color can be actively tuned by switching the Sb_2S_3 between the amorphous and crystalline states. The metasurface of this work gives a novel platform for the reconfigurable structural color, inspiring diversiform application of high-resolution screens, vivid printing, optical encryption, and even high-density data storage.

1. Introduction

Structural colors arising from the interference, diffraction, and scattering effects between incident light and structures are widespread in nature, such as the wings of butterflies, the skin of chameleons, and the feathers of peacocks, etc.[1] Structural color has demonstrated its important application potential in the fields of nano-printing and screen displays for its significant advantages such as more vivid colors under sunlight, higher resolution, and outstanding durability in high-temperature and intense illumination environments.[2] Compared with chemical dye printing, structural colors provide enhanced resolution and superior resistance to fading and degradation. In particular, structural colors exhibit significantly greater chemical stability than chemical dyes at high temperatures and do not bleach when exposed to UV light.[3] Moreover, displays utilizing structural colors have a significantly longer lifespan compared to those using mainstream technologies like liquid crystal display (LCD), light emitting diode (LED), and organic light emitting diode (OLED).[4] Therefore, structural colors have shown an irreplaceable value in the field of innovative colorful pattern printing and display technologies. The mainstream technological approaches to achieving structural color include thin-film interference, diffraction grating, and photonic crystals.[5] However, due to bulk effects, achieving high-quality colors necessitates more particles, larger periodicity, and added layers, resulting in color structure thicknesses substantially exceeding the wavelength and thus limiting the improvement of its resolution. In addition, the colors of these devices are fixed after being fabricated, hindering their suitability for dynamic color displays.[3]

The emergence of metasurfaces has provided a novel technological pathway for the innovative design and functional development of structural colors.[6] On the one hand, the sub-wavelength structures of metasurfaces can significantly improve the pattern resolution of structural colors. On the other hand, by utilizing active metasurfaces with tunable optical response, dynamic modulation of structural colors can be realized, providing a more flexible approach for controlling color displays.[7] Achieving dynamic tunability of structural colors using active metasurfaces depends on effectively controlling the optical properties of the materials and the configuration of the unit structures. Specifically, the former strategy can be realized by introducing functional materials to metasurfaces. For example, Lee et al. modulated the color of transmitted light by controlling the surface plasmon resonance modes of a metallic hole array via liquid crystal molecular orientation manipulation.[8] Shu et al. achieved the modulation of multiple colors through the control of the phase transition of VO_2.[9] While the control of the configuration of the

R. Pan, C. Li, Z. Tang, J. Tan, B. Wang, H. Yang, J. Li
Beijing National Laboratory for Condensed Matter Physics
Institute of Physics
Chinese Academy of Sciences
Beijing 100190, China
E-mail: wangbo2014@iphy.ac.cn; jjli@iphy.ac.cn
Z. Tang, J. Tan, J. Li
School of Physical Sciences
University of Chinese Academy of Sciences
Beijing 100049, China

The ORCID identification number(s) for the author(s) of this article can be found under https://doi.org/10.1002/admt.202500296

DOI: 10.1002/admt.202500296

structural units can be accomplished by stretching the flexible substrate, which has been experimentally verified to enable dynamic modulation of structural colors.[10] The aforementioned strategies provide excellent technical solutions for the development of tunable metasurface structural colors. However, these approaches exhibit the volatile modulation attribute, where the maintenance of color display relies on continuous external stimulation. This results in higher power consumption and a greater risk of color exhibition instability. Therefore, developing non-volatile tunable metasurface structural color devices is of great significance.

Chalcogenide phase-change materials (CPCMs) are characterized by non-volatile phase transitions, where the post-transition state can be maintained stably for decades without external stimulation.[11] Furthermore, CPCMs offer advantages including a rapid phase transition response time (≈100 ns), numerous reversible cycles (≈10^9), and a significant optical contrast induced by the phase transition.[12] These features make CPCMs ideal functional materials for realizing tunable structural colors.[13] Notably, the brightness of structural colors depends on the intensity of reflected/transmitted light from the metasurface. Compared to common CPCMs such as $Ge_2Sb_2Te_5$ (GST) and $Ge_2Sb_2Se_4Te$ (GSST), Sb_2S_3 exhibits a wider bandgap and lower optical losses,[14] which allows a broader range of transparent windows for spectrum modulation in the visible region. The metasurfaces based on Sb_2S_3 have been demonstrated to realize dynamic wavefront modulation[15] and tunable Mie resonances[7b] in the visible region. Consequently, using Sb_2S_3 as the material for tunable metasurfaces can minimize losses in the light-filtering process, thus increasing the brightness of structural colors.

In this work, we proposed and experimentally demonstrated a tunable CMY (cyan, magenta, and yellow) structural color scheme based on Sb_2S_3 metasurfaces, which is composed of a continuous metallic reflector and arrays of sandwiched nanopillar. Compared with the additive color model of RGB, the subtractive color model of CMY is more suitable for reflective metasurface structural color schemes. In addition, the manipulation of the CMY subtractive color spectrum also aligns with the strategy of resonant absorption control in CPCMs metasurfaces. The optimized metasurfaces with the desired size produce structural colors of cyan, magenta, and yellow, respectively. On that basis, non-volatile color modulation of CMY is achieved by Sb_2S_3 phase transition-induced strength and wavelength regulation of the magnetic dipole resonances within the metasurface units. Although there are works that have shown the importance of Sb_2S_3 on structural color[16] the experimental demonstration of this capacity is still challenged for the fabrication of the patterned Sb_2S_3 film is hardly achieved. However, the designed metasurface can be easily fabricated for the PCM in the sandwiched nanopillar is protected by the SiN_x. And the active regulation of the structural color was experimentally validated. The scheme provides additional degrees of freedom for the modulation of structural colors, which allows the color to remain stable over an extended period after phase transition. These results reveal its vast potential for applications in the field of dynamic color exhibition.

2. Device Design and Working Principle

It is crucial to reasonably select a suitable material for active tunable structural color. Figure S1 (Supporting Information) depicts the refractive index and extinction coefficient of different kinds of CPCMs, and Sb_2S_3 stands out naturally for its lower extinction coefficient and optical loss than the others. Following this material system, we design metasurfaces for structural colors, which are schematically shown in **Figure 1a**. The cyan, magenta, and yellow structure colors are selected as the exhibition colors. For the metasurfaces, the silicon wafer is chosen as the substrate to support the upper structures. Au film that serves as the reflective layer lies on the top of the silicon substrate. Here, Au was chosen for its absorption can suppress the high-order resonance in the blue band, whose absorption was also considered in the investigation of the structural color. The processable characteristic should be considered that the Sb_2S_3 is a type of fragile material, which is easily damaged by the alkaline developer and the chemical environment during the etching. Thus, protective layers such as SU-8 polymer or SiO_2 film have been used for its patterning process. Here, we introduced a sandwiched configuration, where a Sb_2S_3 film is sandwiched by SiN_x films, as the unit cell. Here, the protective layer is chosen as SiN_x not only for its stable chemical properties but also as an integral component of the metasurface to achieve targeted optical responses. The three upper patterned layers ($SiN_x/Sb_2S_3/SiN_x$) form an array of sandwiched nanopillar. To prevent oxidation of Sb_2S_3 and the volatilization of sulfur atoms during the phase transition, the metasurface structures are covered with a 15 nm thick Al_2O_3 conformal protective layer. The unit cells of the metasurfaces possess C_{4v} symmetry, rendering the metasurface insensitive to the incident light's polarization state. All the geometric parameters can be found in Figure 1b, from top to bottom, the thickness of each layer of the metasurface has been fixed to the top layer of SiN_x of $H_1 = 110$ nm, Sb_2S_3 of $H_2 = 40$ nm, the bottom layer of SiN_x of $H_3 = 110$ nm, and Au reflector of $H_4 = 100$ nm, respectively. The length and period of the nanopillars are labeled as L and P, respectively. The light-filtering characteristics of the metasurface can be controlled by artificially adjusting the size of L and P, thereby enabling the reflected light to exhibit different colors. The phase change of the PCM can be easily achieved by a thermal process of not more than 300 °C, Figure 1c clearly shows the microscopy images of the Sb_2S_3 film before and after the annealing process. Domains can be observed for the processed film distinct from the unprocessed one, showing that we have successfully manipulated the Sb_2S_3's phase change.[17] A Sb_2S_3 film 50 nm thick, which shows a green color due to the film interference, was deposited on a Si substrate to demonstrate the phase change of the PCM. In addition, atomic force microscopy (AFM) and energy-dispersive X-ray spectroscopy (EDS) are sequentially employed to characterize the surface roughness and element ratios of the Sb_2S_3 films. The measured results are shown in Figures S2 and S3 (Supporting Information), indicating a flat surface as well as uniform and accurate element composition. By selecting appropriate structural parameters, the cyan, magenta, and yellow (CMY) structural colors were realized. On that basis, the reflection spectra of the metasurface would change after the phase state of Sb_2S_3 changed from

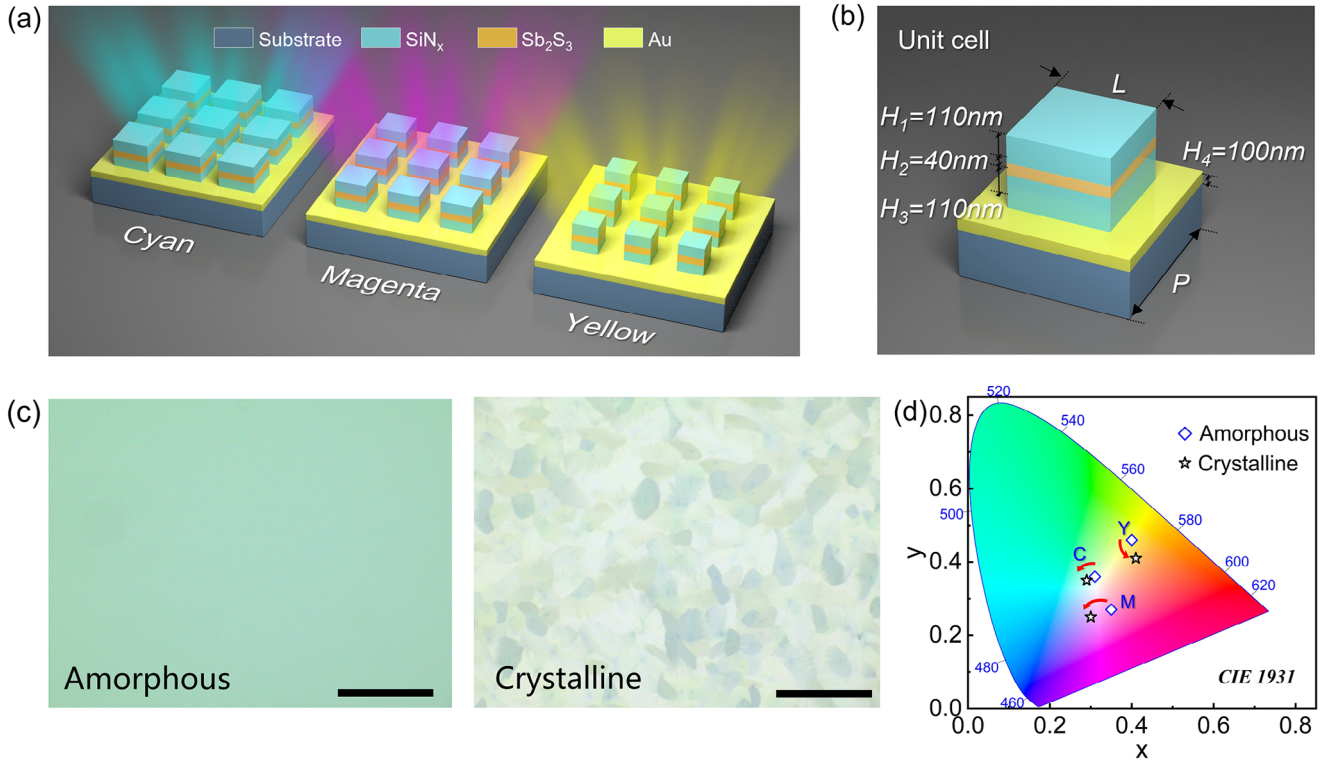

Figure 1. Schematics of the metasurfaces and corresponding structural colors. a) Schematic diagrams of the Sb_2S_3-based metasurfaces for CMY structural colors. b) Schematic of unit cells of the metasurfaces, where the length and period of the nanopillars are labeled as *L* and *P*, and from top to bottom, the thickness of each layer of the metasurface have been fixed to top layer of SiN_x of $H_1 = 110$ nm, Sb_2S_3 of $H_2 = 40$ nm, bottom layer of SiN_x of $H_3 = 110$ nm, and Au reflector of $H_4 = 100$ nm, respectively. c) Microscopic optical images of the amorphous and crystalline Sb_2S_3. Scale bar: 50 µm. d) The CIE chromaticity diagram plot for structural colors.

the amorphous state to the crystalline state, which is visually illustrated in the CIE chromaticity diagram plot in Figure 1d. So far, the design of a Sb_2S_3 metasurface-based tunable CMY structural color device has been completed.

Numerical simulations were performed using finite-domain time-difference (FDTD) method. Detailed parameter settings used in the simulation calculations are illustrated in the experimental section. First, a sandwiched nanopillar with $L = 180$ nm and $P = 360$ nm was built to reveal the behind physics the active color modulation. **Figure 2**a depicts the reflected spectra of both the metasurfaces with amorphous and crystalline Sb_2S_3 where the incidence was an x-polarized light that illuminated the top of the metasurface (Figure 2b). As a comparison, Figure S4 (Supporting Information) shows the transmission curves of the metasurface with the same feature sizes but an Ag reflector, it can be clearly seen that there are peaks in the high-frequency band, which refer to the high-order resonances of the metasurface. However, the peaks are hardly recognized for the metasurface of Au reflector (Figure 2a), indicating that Au can effectively suppress the high-order resonance. Despite the profile of the reflection of Au film, a dip in the reflected spectra that means a high absorption at the corresponding wavelength can be found. The displayed hue of the color is determined by the above-mentioned absorption, which is consistent with the principle of the subtractive mixture of colors that has been widely used in printing and dyeing. Thus, we introduce the CMY that is the most important primary color in the subtractive mixture of colors to highlight the performance of our structural color metasurface. What is more, it is clearly seen that the amplitude experiences a prominent decrease with the material changes from the amorphous state to the crystalline, which enables an active manipulation of structural color. The localized electrical and magnetic field of a cross-section along the Sb_2S_3 layer was extracted in Figure 2c–e. The magnetic field distribution of the amorphous metasurface depicts a maximum at the center of the structure and spread along the *y*-axis. The electrical field along the *z*-axis shows the opposite sign, indicating an annular displacement current, which is the typical property of a magnetic dipole. Contrary to the amorphous state, Figure 2e shows the magnetic field distribution of the metasurface with crystalline Sb_2S_3. A dramatic decrease in field strength along *x*-*y* planes can be recognized, which is consistent with the magnetic field variation behavior along *x*-*z* planes (Figure S5, Supporting Information). The decrease of the magnetic field comes from a smaller displacement current. Finally, the optical response of the active metasurface is schematically revealed in Figure 2f. As for the amorphous state, the Sb_2S_3 demonstrates a low intrinsic loss, resulting in a large displacement current that contributes to a high reflectance. However, when it comes to the crystalline state, the enlarged material loss cut the path of displacement current, and the light was consumed in the phase change material layer, resulting in a low reflectance. The change of reflectance further influences the observed color of the

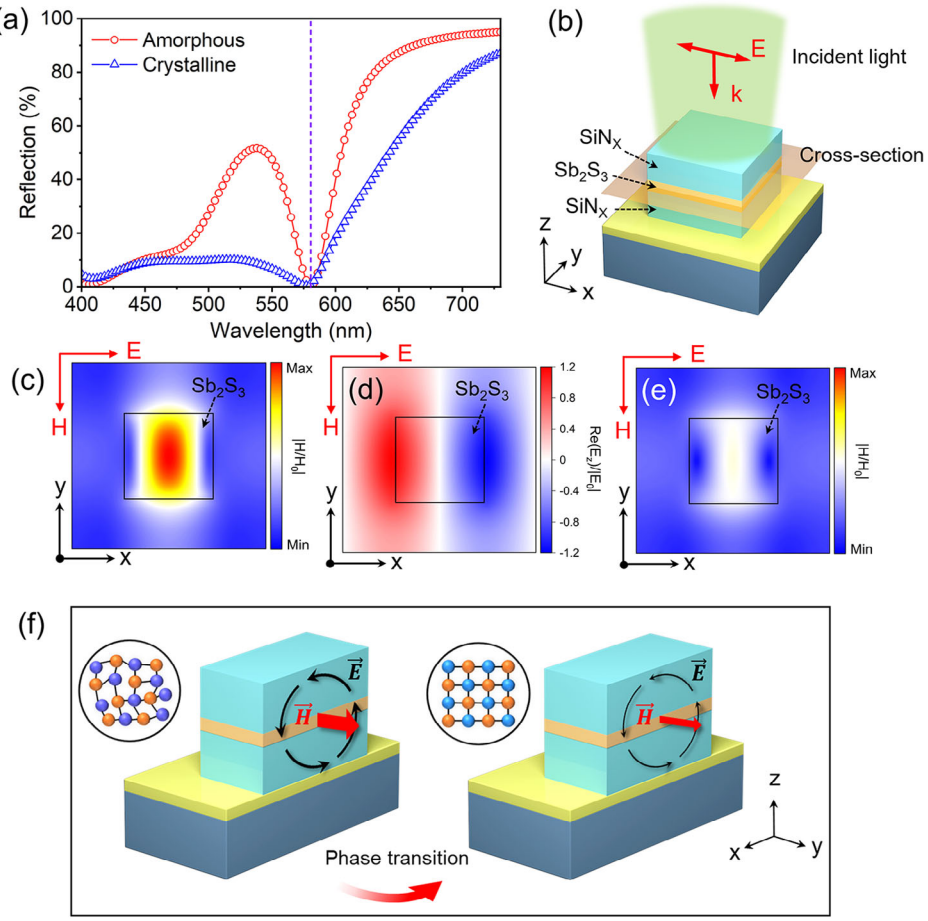

Figure 2. The physical mechanism of active manipulating structural color. a) Curves of simulated reflected spectra of an array of nanopillar with L = 180 nm and P = 360 nm with amorphous (red curve) and crystalline (blue curve) Sb_2S_3; b) Schematical illustration of the simulation, where the light comes forward, and the magnetic field c) and electrical field along z-axis d) distributions of amorphous state and the magnetic field e) distribution of crystalline Sb_2S_3 are extracted; f) The displacement current and magnetic dipole strengths' evolution with the phase change process.

metasurface, giving a potential means to manipulate structural color on demand.

3. Results and Discussion

Metasurfaces with different side lengths and pitches are simulated to prove the superior spectrum regulation property after the optical response mechanism is clarified. As Figure S6 (Supporting Information) shows, both the resonance position and the reflection can be effectively regulated by the configuration of unit cells, and a large contrast between the crystalline and amorphous Sb_2S_3 can be observed, paving the way for active modulation of structural color. The metasurfaces with distinctive configurations are fabricated following the process shown in Figure S7 (Supporting Information), which consists of the physical/chemical vapor deposition (PVD/CVD), e-beam lithography (EBL), and the reactive ion etching (RIE) process. A series of metasurfaces was fabricated following the above-mentioned method to highlight the color modulation ability, Figure S8 (Supporting Information) shows the microscopic image of the metasurface with different configurations and phase states, which depicts abundant color with a large modulation range and color modulating capacity with phase change. The metasurfaces with displayed colors of cyan, magenta, and yellow with critical dimensions of P = 360 nm, L = 170 nm (**Figure 3a**), P = 320 nm, L = 160 nm (Figure 3b), and P = 240 nm, L = 150 nm (Figure 3c) are fabricated to investigate the spectra modulation ability. The spectra of the metasurface with Sb_2S_3 in an amorphous state can be directly measured, while that of crystalline state can be easily collected by an annealing process under a temperature of 300 °C. Simulated results corresponding to the configurations can be obtained in Figure 3d–f, showing that the intensity of reflection decreasing with the phase of Sb_2S_3 changes from amorphous to crystalline state that in line with the previous predictions, resulting in the active modulation of both the hue and the brightness of the structural color. Where the dip of the reflected spectra, which is related to the absorbed band of the metasurface, redshifts from the blue band to the green and red band, respectively. One can imagine that the three configurations show yellow, magenta, and cyan in color based on the subtractive color mixture. For example,

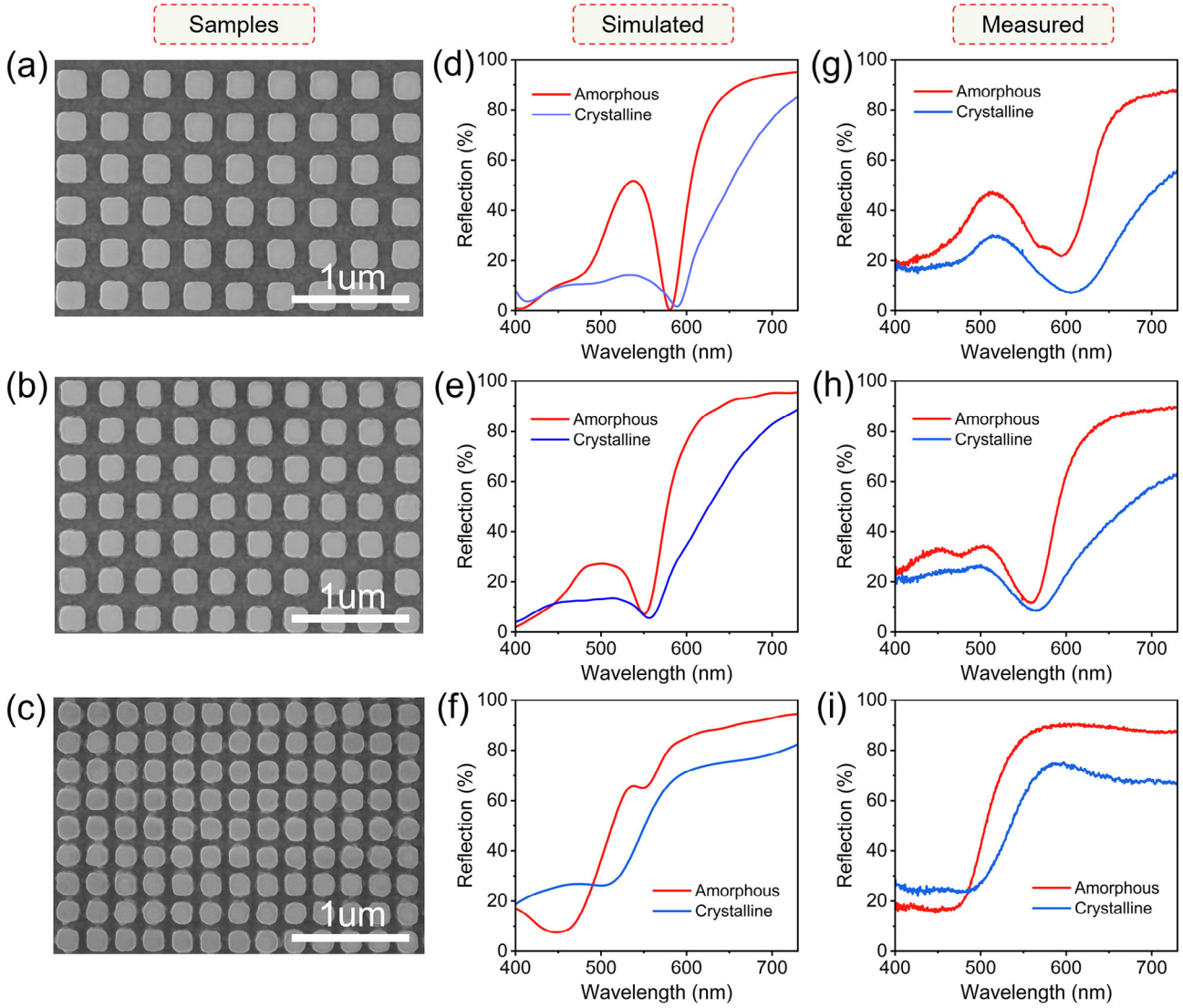

Figure 3. The fabrication of structural color metasurface with its spectra. SEM images of metasurface with a) $P = 360$ nm, $L = 170$ nm, b) $P = 320$ nm, $L = 160$ nm, and c) $P = 240$ nm, $L = 150$ nm; d–f) are corresponding reflected spectra by simulation, and the experimental results can be seen in g–i).

yellow equals the subtraction of white (light source) and blue (absorption). Experimental results confirm the validity of the design, thanks to the fabricated metasurface having the same structure as the design in both the x-y plane and the z-direction (Figure S9, Supporting Information), collected spectra shown in Figure 3g–i depict consistent curves with the simulations. The effective regulation of the spectrum by both the configuration and the phase of the Sb_2S_3 metasurface enables the large range controllability of the structural color.

Since the spectrum regulation capacity has been confirmed, a microscope with a 5× objective is introduced to determine the displayed color of the metasurface experimentally. **Figure** 4a depicts the collected spectra and the corresponding structural color of the metasurface shown in Figure 3, and the insets are observed colors of the metasurface, which show typical colors of cyan, magenta, and yellow, respectively, indicating the strong color regulation of the configuration of the sub-wavelength resonator. As for the color yellow, a dip can be found in the short wavelength band, meaning that the blue light was absorbed. And with the configurations of the metasurface changing, the dip experienced a redshift, and the magenta and cyan were obtained, respectively. Importantly, the phase change of Sb_2S_3 gives a possibility to actively tune the color even when the structure of the metasurfaces has been fixed. We utilize a rapid annealing process to induce the phase change of the Sb_2S_3, corresponding spectra can be found in Figure 4b. The reflection of the metasurfaces is shrunk and a redshift can be observed, in the color, the color becomes darker, and the hue also changes in some content. To intuitively understand this phenomenon, Figure 4c counts the color in the HSB (hue, saturation, and brightness) space, where the brightness change can be clearly seen in the left image, while the change of hue and saturation can be observed in the right one. The experimental

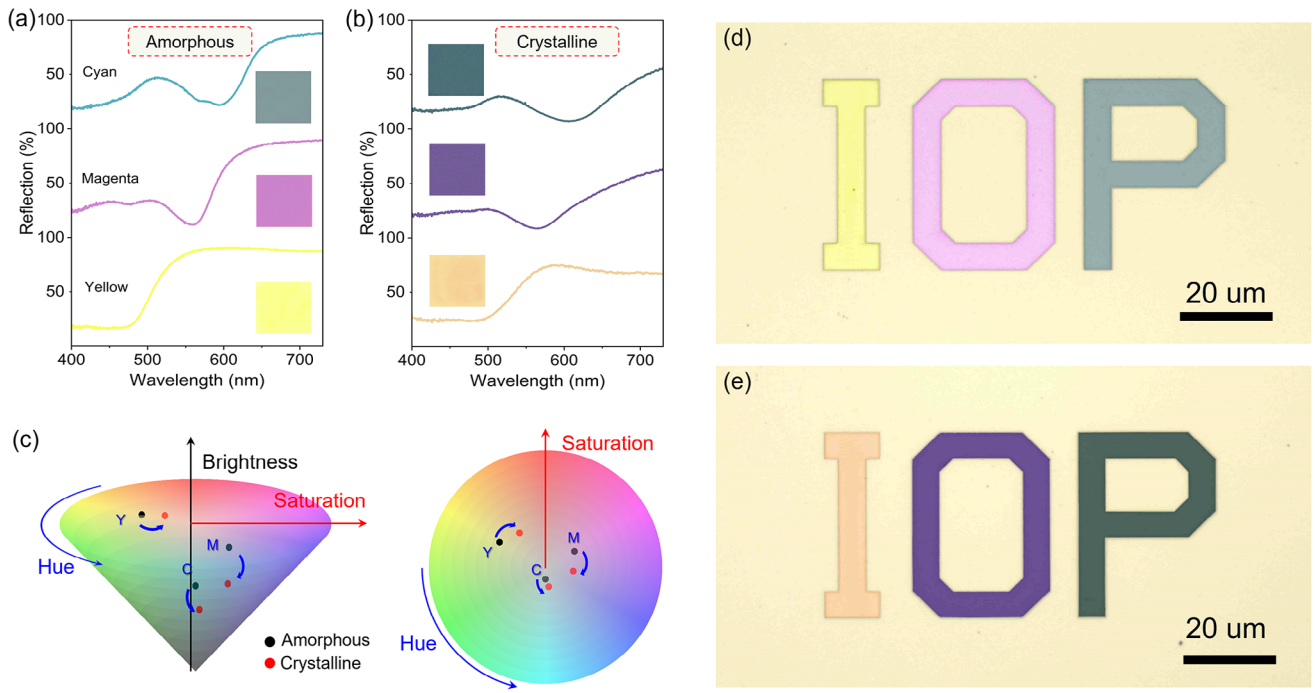

Figure 4. The active control of structural color. a,b), the reflected spectra with the displayed color of the chosen metasurfaces with amorphous and crystalline Sb_2S_3; c) The color change of the metasurface in the HSB color space; d,e), Color microscopic images of the letters "I," "O," and "P" with metasurface of different configurations and phase states, respectively.

results indicate that our metasurface provides a novel method to control the structural color, helping the realization of reconfigurable color display and high-resolution printing. Here, we use the letters "I," "O," and "P" to verify the high performance of the PCM-based metasurface, Figure 4d depicts the optical microscopic image of the metasurface under amorphous state, where the three letters hold the color of yellow, magenta, and cyan. The background of the pattern is buff, originating from the gold layer, which shows weak reflection at the high-frequency band, underneath the sandwiched nanostructures. With the Sb_2S_3 changes from the amorphous to crystalline state, the color of the background remains unchanged, but the colors of the patterned layer are obviously distinct from the amorphous state, highlighting the crucial role of CPCM in achieving active structural color.

4. Conclusion

In conclusion, we have designed a metasurface consisting of a layer of metallic reflectors and an array of sandwiched subwavelength nanopillar. Both the configuration of the nanoresonator and the phase state of Sb_2S_3 contribute to the finally displayed color, where the former determines the hue of the color by regulating the magnetic dipole, while the latter enables the reconfiguration of hue and brightness of structural color even the structure is fixed. The CMY primary colors are selected to verify the active tunability of the color, showing that the brightness and the hue can be effectively modulated. A pattern with various colors was constructed by the designed metasurface and proved that the structural color metasurface can be applied in dynamic displays. Importantly, the structure color can be further improved by introducing new concepts of optical response such as bound states in the continuum,[18] optimizing the configuration of the unit cell, and choosing a more powerful reflector. The device toward subtractive structural colors not only paves the way for applications including high-resolution printing and vivid display, but also inspires the design of a series of reconfigurable optical components on micro and nano scale.

5. Experimental Section

Numerical Simulation: The optical reflection spectra and electromagnetic field profiles of the designed metasurfaces were simulated using the FDTD method. The periodic boundary condition was adopted along both x and y in-plane directions and perfectly matched layers (PML) boundary condition was set along the propagation of electromagnetic waves (out-of-plane z-direction). A uniform grid with maximum mesh steps of 10 nm along the x and y directions and 4 nm along the z-direction was used to discretize the simulation region. An x-polarized plane wave was launched incident to the unit cell along the z-direction.

Device Fabrication: The silicon plates with a thickness of 500 µm were chosen as the substrate to support the upper nanostructures. Prior to fabrication, the substrates were ultrasonically cleaned in acetone, isopropanol, and ultrapure water, and subsequently dried with nitrogen flow. The devices were subsequently fabricated according to the following steps. First, the 5 nm Ti and 100 nm Au films were successively deposited on the substrate by electron beam evaporation (EBE). Subsequently, the 110 nm SiN_x, 40 nm Sb_2S_3, and 110 nm SiN_x films were deposited in turn. The deposition of SiN_x film was performed by inductively coupled plasma enhanced chemical vapor deposition (ICPECVD) at 130 °C, during which the gas flow rates of SiH_4, NH_3, and Ar were 6.5, 11, and 249 sccm, respectively. The deposition pressure was kept at 22.5 mTorr with ICP power of 300 W. The Sb_2S_3 film was deposited using the magnetron sputtering (MS)

method at room temperature. The deposition process was performed using a synthesized single target with an Ar gas flow rate at 10sccm, chamber pressure at 7 mTorr, and sputtering radio frequency power of 50 W. Then, the negative photoresist (AR-N 7520) was spin-coated on the top of the Sb_2S_3 film at 6000 rpm and pre-baked at 85 °C for 1 min at the hotplate. After that, the electron beam lithography (EBL) process with an accelerating voltage of 100 KV, 2 nA beam current, and dose of 200 μm cm^{-2} was employed to write the exposure pattern on the photoresist. The desired pattern was thus obtained after developing in AR 300–46 solution. Afterward, the reactive ion etching (RIE) was performed with a gas mixture of CHF_3:O_2 (10:1) with respective flow rates of 50 and 5 sccm, chamber pressure of 55 mTorr, and RF power of 200 W. Then, the photoresist masks were removed using RIE with oxygen plasma with an O_2 flow rate of 50 sccm, pressure of 100 mTorr, and RF power of 50 W. Finally, the conformal Al_2O_3 film with a thickness of 15 nm was deposited using the atomic layer deposition (ALD) at 150 °C for protection.

Measurement: A homemade optical test platform with a halogen light source (HL2000) was introduced to collect the reflective spectra of the metasurface, and the spectrometer (PG 2000) working in the visible region was used to collect the reflective signal. Due to the extremely high reflection, the reflection signal of Ag mirrors was used as the reference. The SEM photographs were taken on Hitachi Regulus 8230 with an accelerating voltage of 10 KV and a beam current of 7 nA. The elementary compositions of the Sb_2S_3 films were obtained through EDS (Ultim Max, Oxford) analysis. The roughness of the Sb_2S_3 films was characterized by AFM (Dimension Edge, Bruker). The refractive index and extinction coefficient of Sb_2S_3, GSST, and GST were measured on a spectral ellipsometer (ME-Mapping). The colorful micrography of the metasurface was collected by a CCD camera with a 5× objective lens.

Supporting Information

Supporting Information is available from the Wiley Online Library or from the author.

Acknowledgements

R.P. and C.L. contributed equally to the work. This work was supported by the National Key Research and Development of China (Grant Nos. 2023YFF0721901 and 2023YFF0715902), the National Natural Science Foundation of China (Grant Nos. 12074420, U21A20140, 12304463, and 12204527), the Chinese Academy of Sciences through the Project for the Young Scientists in Basic Research (YSBR-021). This work was also technically supported by Beijing Metasurface Optics Device Generic Technology Platform, and Synergetic Extreme Condition User Facility (SECUF, https://cstr.cn/31123.02.SECUF).

Conflict of Interest

The authors declare no conflict of interest.

Data Availability Statement

The data that support the findings of this study are available from the corresponding author upon reasonable request.

Keywords

dynamic modulation, low loss, phase change materials, subtractive structural color, tunable metasurface

Received: February 20, 2025
Revised: May 19, 2025
Published online: May 31, 2025

[1] a) Y. L. Fu, C. A. Tippets, E. U. Donev, R. Lopez, *Wires Nanomed. Nanobi.* **2016**, *8*, 758; b) Y. H. Gu, L. Zhang, J. K. W. Yang, S. P. Yeo, C. W. Qiu, *Nanoscale* **2015**, *7*, 6409; c) S. D. Rezaei, Z. G. Dong, J. Y. E. Chan, J. Trisno, R. J. H. Ng, Q. F. Ruan, C. W. Qiu, N. A. Mortensen, J. K. W. Yang, *ACS Photonics* **2021**, *8*, 18.

[2] R. Fu, K. Chen, Z. Li, S. Yu, G. Zheng, *Opto-Electron. Sci.* **2022**, *1*, 220011.

[3] B. Yang, H. Cheng, S. Q. Chen, J. G. Tian, *Mater. Chem. Front.* **2019**, *3*, 750.

[4] a) H. W. Chen, J. H. Lee, B. Y. Lin, S. Chen, S. T. Wu, *Light:Sci. Appl.* **2018**, *7*, 17168; b) E. L. Hsiang, Z. Y. Yang, Q. Yang, Y. F. Lan, S. T. Wu, *J. Soc. Inf. Display* **2021**, *29*, 446.

[5] L. Li, Z. Yu, C. Ye, Y. Song, *Adv. Funct. Mater.* **2024**, *34*, 2311845.

[6] a) Y. Gu, L. Zhang, J. K. Yang, S. P. Yeo, C.-W. Qiu, *Nanoscale* **2015**, *7*, 6409; b) Z. Dong, J. Ho, Y. F. Yu, Y. H. Fu, R. Paniagua-Dominguez, S. Wang, A. I. Kuznetsov, J. K. W. Yang, *Nano Lett.* **2017**, *17*, 7620; c) Y. Nagasaki, M. Suzuki, J. Takahara, *Nano Lett.* **2017**, *17*, 7500; d) W. Yang, S. Xiao, Q. Song, Y. Liu, Y. Wu, S. Wang, J. Yu, J. Han, D. P. Tsai, *Nat. Commun.* **2020**, *11*, 1864; e) X. Zhu, W. Yan, U. Levy, N. A. Mortensen, A. Kristensen, *Sci. Adv.* **2017**, *3*, 1602487; f) Z. Dong, L. Jin, S. D. Rezaei, H. Wang, Y. Chen, F. Tjiptoharsono, J. Ho, S. Gorelik, R. J. H. Ng, Q. Ruan, C.-W. Qiu, J. K. W. Yang, *Sci. Adv.* **2022**, *8*, abm4512.

[7] a) J. H. Yang, V. E. Babicheva, M. W. Yu, T. C. Lu, T. R. Lin, K. P. Chen, *ACS Nano* **2020**, *14*, 5678; b) L. Lu, Z. G. Dong, F. Tijiptoharsono, R. J. H. Ng, H. T. Wang, S. D. Rezaei, Y. Z. Wang, H. S. Leong, P. C. Lim, J. K. W. Yang, R. E. Simpson, *ACS Nano* **2021**, *15*, 19722; c) C. R. de Galarreta, I. Sinev, A. M. Alexeev, P. Trofimov, K. Ladutenko, S. G. C. Carrillo, E. Gemo, A. Baldycheva, J. Bertolotti, C. D. Wright, *Optica* **2020**, *7*, 476.

[8] Y. Lee, M. K. Park, S. Kim, J. H. Shin, C. Moon, J. Y. Hwang, J. C. Choi, H. Park, H. R. Kim, J. E. Jang, *ACS Photonics* **2017**, *4*, 1954.

[9] F. Z. Shu, F. F. Yu, R. W. Peng, Y. Y. Zhu, B. Xiong, R. H. Fan, Z. H. Wang, Y. M. Liu, M. Wang, *Adv. Opt. Mater.* **2018**, *6*, 1700939.

[10] M. L. Tseng, J. Yang, M. Semmlinger, C. Zhang, P. Nordlander, N. J. Halas, *Nano Lett.* **2017**, *17*, 6034.

[11] a) D. Lencer, M. Salinga, B. Grabowski, T. Hickel, J. Neugebauer, M. Wuttig, *Nat. Mater.* **2008**, *7*, 972; b) M. Wuttig, H. Bhaskaran, T. Taubner, *Nat. Photonics* **2017**, *11*, 465.

[12] a) T. Cao, R. Wang, R. E. Simpson, G. Li, *Prog. Quantum Electron.* **2020**, *74*, 100299; b) C. Zheng, R. E. Simpson, K. Tang, Y. Ke, A. Nemati, Q. Zhang, G. Hu, C. Lee, J. Teng, J. K. Yang, *Chem. Rev.* **2022**, *122*, 15450.

[13] a) P. Prabhathan, K. V. Sreekanth, J. Teng, R. Singh, *Nano Lett.* **2023**, *23*, 5236; b) P. Hosseini, C. D. Wright, H. Bhaskaran, *Nature* **2014**, *511*, 206; c) L. Lu, Z. Dong, F. Tijiptoharsono, R. J. H. Ng, H. Wang, S. D. Rezaei, Y. Wang, H. S. Leong, P. C. Lim, J. K. Yang, *ACS Nano* **2021**, *15*, 19722.

[14] a) W. L. Dong, H. L. Liu, J. K. Behera, L. Lu, R. J. H. Ng, K. V. Sreekanth, X. L. Zhou, J. K. W. Yang, R. E. Simpson, *Adv. Funct. Mater.* **2019**, *29*, 1806181; b) M. Delaney, I. Zeimpekis, D. Lawson, D. W. Hewak, O. L. Muskens, *Adv. Funct. Mater.* **2020**, *30*, 2002447.

[15] P. Moitra, Y. Z. Wang, X. N. Liang, L. Lu, A. Poh, T. W. W. Mass, R. E. Simpson, A. I. Kuznetsov, R. Paniagua-Dominguez, *Adv. Mater.* **2023**, *35*, 2205367.

[16] a) X. Wei, J. Nong, Y. Zhang, H. Ma, R. Huang, Z. Yuan, Z. Zhang, Z. Zhang, J. Yang, *Nanomaterials* **2023**, *13*, 1452; b) O. Hemmatyar, T. Brown, A. Adibi, presented at 2020 Conference on Lasers and Electro-Optics (CLEO) **2020, IEEE, San Jose, CA, USA**. c) Z. R. Omam, B. Khalichi, A. K. Osgouei, A. Ghobadi, M. Khalily, E. Ozbay, presented at 2024 IEEE International Symposium on Antennas and

Propagation and INC/USNC-URSI Radio Science Meeting (AP-S/INC-USNC-URSI) 14–19 July 2024 **2024, IEEE, Firenze, Italy**.

[17] a) Y. Gutierrez, A. P. Ovvyan, G. Santos, D. Juan, S. A. Rosales, J. Junquera, P. Garcia-Fernandez, S. Dicorato, M. M. Giangregorio, E. Dilonardo, F. Palumbo, M. Modreanu, J. Resl, O. Ishchenko, G. Garry, T. Jonuzi, M. Georghe, C. Cobianu, K. Hingerl, C. Cobet, F. Moreno, W. H. P. Pernice, M. Losurdo, *iScience* **2022**, *25*, 104377; b) H. Liu, W. Dong, H. Wang, L. Lu, Q. Ruan, Y. S. Tan, R. E. Simpson, J. K. W. Yang, *Sci. Adv.* **2020**, *6*, abb7171.

[18] a) K. Koshelev, S. Lepeshov, M. Liu, A. Bogdanov, Y. Kivshar, *Phys. Rev. Lett.* **2018**, *121*, 193903; b) Z. Dong, Z. Mahfoud, R. Paniagua-Dominguez, H. Wang, A. I. Fernandez-Dominguez, S. Gorelik, S. T. Ha, F. Tjiptoharsono, A. I. Kuznetsov, M. Bosman, J. K. W. Yang, *Light:Sci. Appl.* **2022**, *11*, 20.